Analytical Thermal Boundary Condition for Quasi-Transient Simulation of Internal Flow Experiments*

Peter R Forsyth †
National Research Council Canada, 1200 Montreal Road, Ottawa, Ontario, Canada

David Gillespie‡ and Matthew McGilvray§
Oxford Thermofluids Institute, University of Oxford, Osney Mead, Oxford, OX2 0ES, UK

Transient thermochromic liquid crystal (TLC) experiments can provide high fidelity spatially-resolved heat transfer data for complex geometries, particularly where infrared techniques cannot be applied. One challenge when applying transient methods to internal geometries is the local definition of the driving gas temperature. The transient nature of the streamwise driving gas temperature profile has led to comparisons with steady state computational fluid dynamics (CFD) being questioned. This paper explores simulating the temporal behaviour of transient TLC experiments directly. A novel technique is developed to account for differences in the gas and solid time scales, where surface temperature is calculated at each spatial location analytically from the surface heat flux using an impulse response method assuming one dimensional, semi-infinite conduction. Post-processing of the simulated surface temperature history is performed using the same method as experimentally, allowing for direct comparison. This analytical thermal boundary condition (ATBC) is applied to simulate a transient TLC experiment of a stationary super-scaled rib turbulated internal cooling passage in a gas turbine engine. Traditional steady state simulations were also performed with constant temporal and spatial temperature boundary conditions. Results show that calculations using the new ATBC and traditional steady state method give very similar Nusselt number distributions and mean values in relation to the experimental data, suggesting the larger discrepancy between simulations and the experiments is not the definition of the driving gas temperature. Analysis of transient variation of Nusselt number indicated brief highly localised maximum variations up to 40 %, though this was not found to significantly affect the mean values, and passage-averaged values converged to within 0.5 % of final value within 0.2 s.

*This paper was in part presented at the AIAA Aviation Forum 2018 (paper no. AIAA 2018-4289). Figures reprinted in part with permission of the authors.

†Corresponding author peter.forsyth@nrc-cnrc.gc.ca. Was Postdoctoral Research Assistant, Oxford Thermofluids Institute, University of Oxford, UK, now Research Officer, National Research Council Canada.

‡Professor, Department of Engineering Science, University of Oxford, Oxford, UK

§Professor, Department of Engineering Science, University of Oxford, Oxford, UK

Nomenclature

A	=	Area
Bi	=	Biot number, $\frac{hl}{k}$
c_p	=	Specific heat capacity at constant pressure
D_h	=	Hydraulic diameter
E	=	Total energy
e	=	Rib height
f	=	Friction factor, $\Delta P \frac{D_h}{2\rho U^2 L}$
H	=	Impulse response function
h	=	Heat transfer coefficient; sensible enthalpy (Eq. 5)
k	=	Thermal conductivity
l	=	Characteristic length
m	=	Mass
Nu	=	Nusselt number, $\frac{h.l}{k}$
P	=	Pressure
Pr	=	Prandtl number, $\frac{\mu c_p}{k}$
p	=	Rib pitch; perimeter
$\dot{q}$	=	Heat flux
r	=	Radius
Re	=	Reynolds number, $\frac{\rho U l}{\mu}$
T	=	Temperature
t	=	Time
U	=	Velocity
x,y,z	=	Coordinates

Subscripts

1	=	Perspex
2	=	Rib
g	=	Gas
init	=	Initial
0	=	Reference
fp	=	Flat plate
p	=	Projected

$q2T_s$	=	Heat flux to surface temperature
s	=	Surface
$T_g 2T_s$	=	Gas temperature to surface temperature
t	=	Turbulent

Greek

α	=	Thermal diffusivity, Rib angle
β	=	Equation 19
θ	=	Non-dimensional surface temperature
λ	=	Direction of curvature
μ	=	Viscosity
ρ	=	Density

Abbreviations

ADI	=	Alternating Direction Implicit
ATBC	=	Analytic thermal boundary condition
AR	=	Aspect ratio, (width/height)
CFD	=	Computational Fluid Dynamics
ERICKA	=	Engine Realistic Internal Cooling Knowledge Applications
FEA	=	Finite Element Analysis
HTC	=	Heat transfer coefficient
LE	=	Leading edge
PS	=	Pressure side
RANS	=	Reynolds-averaged Navier Stokes
SS	=	Suction side
TE	=	Trailing edge
TLC	=	Thermochromic Liquid Crystal

I. Introduction

Measurement of the heat flux on complex surfaces is difficult, particularly for internal geometries found in gas turbine engines. The calculation of spatially-resolved heat transfer coefficients from transient experiments is done by measuring both the driving gas temperature and surface temperature response, typically for a near-step change in the gas temperature [1]. For stationary testing, it is common to initiate the increase in the gas temperature via a fast acting valve system or a heater mesh. The resulting heat flux causes a change in surface temperature. If the experiment is initially held at isothermal conditions, the solid is thick enough, and the geometry has large radius of curvature, the one dimensional Fourier heat conduction equation can to be solved assuming semi-infinite conduction to determine the heat transfer coefficient distribution. Post-processing of the raw data can be undertaken using a variety of techniques including finite difference, analytical derivations [2] and impulse response methods [3]. Corrections for complex geometry exist [4–6] and transient FEA can be applied to truly 3D geometries [7, 8].

For thermochromic liquid crystal (TLC) experiments, surface temperature information comes from imaging TLCs sprayed onto the target surface [2]. The helical structure of the crystals alters with temperature, changing the wavelength of light reflected, *i.e.* the surface colour observed changes with temperature. Although improvements in infrared camera technology have seen a reduction in the application of TLCs for external flow experiments, the difficulties relating to their imaging of internal surfaces has seen continued application of the TLC method. Narrow band liquid crystals have been shown to produce the most robust and accurate experimental technique, particularly if multiple crystals are applied to give information over a wide range of temperatures [9].

Differences in heat transfer coefficient between transient experiments and steady state experiments/CFD, independent of the uncertainties in the experiment, are widely attributed to the following:

- the definition of driving gas temperature
- gas temperature transients over the course of the experiment
- an approximation of one-dimensional conduction
- establishment time of the thermal boundary layer
- changing hydrodynamic conditions in the system
- turbulence modelling

The heat transfer coefficient for internal flow experiments is typically referenced to a driving gas temperature ($\dot{q} = h(T_g - T_w)$) due to the difficulty in adequately measuring the adiabatic recovery temperature [2]. This driving gas temperature is typically measured with small bead thermocouples in the bulk passage flow. Driving gas temperatures are usually measured on the passage centreline to reduce the substantial complexities related to measuring a mixed bulk or mass-averaged value of gas temperature [10]. As this paper aims to reproduce the experimental method numerically as possible, the same definition of gas temperature, centreline, is used.

As a slice of gas convects down the passage, it will drop in temperature due to thermal energy transferred to the solid. As the solid heats up with time, the amount of thermal energy transferred to the solid as the slice of gas convects down the passage decreases. This is in contrast to external flows where a single driving gas temperature history can be applied. Additionally, a perfect step change in gas temperature is physically not possible. To overcome this, experimentalists exhibit extreme care in the use of either convolution strategies (e.g. [3]) or time delayed series solutions of simple gas temperature input profiles to model the substrate behaviour fully during a test. For example: in [11] the local temperature distribution during start-up is not used to determine the HTC, allowing its application in test rigs where there may be transient compression of incoming test gas. In most transient TLC tests, a strategy is used with many fast response thermocouples providing a good description of the spatial and temporal gas temperature distribution and this is used to model the system as a series of steps, ramps [2] or exponential rises in gas temperature [12]. Many experimentalists use the full colour range of wide band crystals [13], or the non-dimensionalised intensity history [14] to introduce redundancy into the solution of the system of equations.

The significance of three dimensional conduction effects can be assessed by post processing of the one dimensional results to determine a pseudo value of:

$$\frac{\partial^2 \dot{q}}{\partial x_1^2} \ll \frac{\dot{q}}{2\alpha t} \quad \text{and} \quad \frac{\partial^2 \dot{q}}{\partial x_2^2} \ll \frac{\dot{q}}{2\alpha t} \tag{1}$$

where x_1 and x_2 are the axial and spanwise directions in a local coordinate frame [6]. Approaches such as the three dimensional Alternating Direction Implicit (ADI) method have been used to correct the output from the one dimensional solution [6], and corner corrections [5]. More recently, this has been superseded by full three dimensional analyses due to increased computational capacity [8].

Another consideration is what effect does the transient change in the thermal boundary layer has on the local heat transfer coefficient, which in a transient TLC experiment will be continually changing. Cukurel and Arts [15] demonstrated this is significant by comparing two steady state cases of an iso-heat flux and a convective boundary condition. This has led to strategies applying three point non-linear corrections when applying steady state CFD to determine local heat transfer coefficients [16].

The comparison between HTC values derived from transient experiments and steady-sate CFD is still questioned. Sathyanarayanan and Shih [17] reported very large differences between HTC determined from transient conjugate heat transfer simulations, with a variance of 30% in HTC reported. Unfortunately, an over-simplification of the experimental data reduction scheme was applied where multi-dimensional effects at sharp corners and spatial variation in the reference gas temperature down the passage were not treated appropriately, as described above. Thus, the magnitude of the discrepancies in HTC are likely to be smaller than reported.

This paper details and demonstrate the novel application of a quasi-transient analytical thermal boundary condition (ATBC) technique for numerically simulating the transient technique used by experimentalists to measure heat transfer coefficients. This ATBC approach allows the simulations to capture both the rise in wall temperature and provides the same definition of gas temperature used experimentally. It uses CFD to solve the fluid and the heat flux distribution, with the surface temperature then calculated analytically from incident surface heat flux by applying the impulse response method to solve the semi-infinite one-dimensional conduction equation. The ATBC simulations are compared to both TLC experimental data from a rib roughened passage [18], and also steady state CFD, carried out to industry standard. This paper also redresses some of the conclusions drawn in [17] and provides a true assessment of HTC values

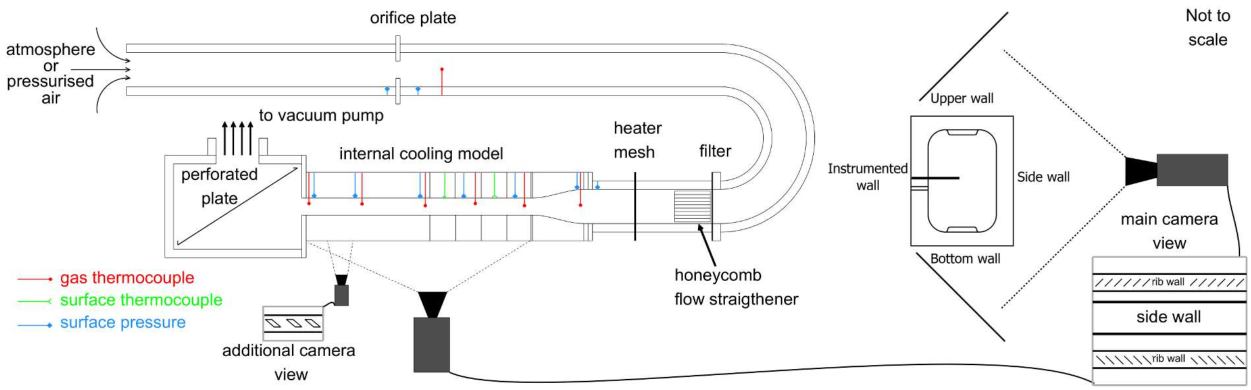

Fig. 1 Schematic of experimental setup of flow path, instrumentation and camera view [19]

determined by steady state CFD with a spatially and temporally uniform thermal boundary condition in comparison to HTC values determined from experimental transient TLC testing in a rib turbulated passage. It is demonstrated that though brief transient variations of HTC up to 40% are seen, these do not significantly effect mean values when an appropriate processing method is applied, which are seen to converge quickly.

II. Stationary Internal Cooling Passage Experiments

The experimental data simulated in this paper are from an aspect ratio 1:3 super-scaled rib roughened internal cooling passage [18, 19]. The geometry is typical of that found in a modern gas turbine engine blade. The experiment employed the transient TLC technique to capture surface heat transfer coefficient data, using a near step change in driving gas temperature from initial isothermal ambient conditions from a heater mesh at inlet. The solid walls were made from Perspex thick enough to ensure the semi-infinite conduction. Some of the ribs were manufactured from brass and adhered to the Perspex substrate to enable an average measurement of HTC over the rib. A schematic of the experiment is shown in Figure 1.

The experiment used three narrow band TLCs at nominal activation temperatures of 25, 30 and 35 ^{o}C. The passage is made from Perspex, which has a thermal product of 569 W/m^2.s$^{0.5}$.K and is thick enough over the 30 second test time for the external surface to remain at the initial isothermal condition. Gas temperature was measured on the centreline at five locations using K-type thermocouples, TC1 (upstream) - TC5 (downstream). The data presented in this paper is unwrapped using the nomenclature in Figure 2, where the terms ‘pressure/suction surface’ and ‘leading/trailing edge’ relate to the turbine blade’s outer surfaces in the main gas path, and not the local aerodynamics within the cooling passage. Further details of the experimental setup can be found in [18, 19].

A. Geometry

The internal cooling passage test section consists of a 432 mm long filleted rectangular duct with rib turbulators on two opposing walls (suction and pressure surfaces). The remaining walls (leading and trailing edges) are smooth. The

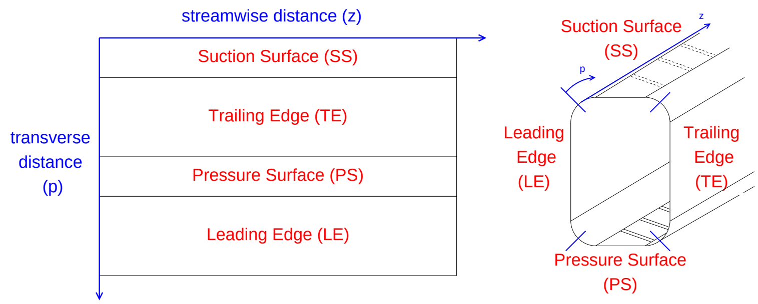

Fig. 2 Passage surface unwrapping and nomenclature [19]

passage has an aspect ratio (width:height) of 1:3 with a rib blockage (e/D_h) of 6.2% and a hydraulic diameter of 29.0 mm. The passage width is 18.66 mm. Ribs in the passage are: at an angle (α) of 45° to the streamwise direction; a pitch to height spacing (P/e) of 10; filleted along all edges (radius of filleting is $e/2$); centred in the passage; span half the width of the passage; staggered by half the pitch between the suction and pressure surfaces; have a 0.9 mm base which is fully recessed into the passage wall; and are made of brass. Both ribbed walls have 24 ribs. HTC data was collected on all four walls. Further discussion is given in [18].

B. Flow Conditions

The majority of this paper focuses on conditions of a passage Reynolds number of 60 000, based on hydraulic diameter. This was set using pressure inlet and outlet conditions to target a mass flow rate of 40 g/s. The initial isothermal temperature was 293 K, with the transient centreline temperature profile measured with thermocouples (Figure 3). The absolute pressure in the passage was set to approximately 1 bar. Upon initiation of the driving gas temperature step, the mass flow rate and Reynolds number decreased by 7.1 % over the experimental time. Reynolds numbers and Nusselt numbers reported were calculated from the gas viscosity based on the most downstream centreline gas thermocouple, TC5, averaged over the test time, as per the experimental method. Further simulations presented at the end of the paper are conducted at passage Reynolds numbers of 19 000 and 107 000.

III. Simulation Setup, Mesh and Sensitivity

A. Governing equations

Flow solution was carried out using commercial code ANSYS Fluent 18.2, a finite volume solver, in an inertial reference frame. The general equations for conservation of mass,

$$\frac{\partial \rho}{\partial t} + \nabla \cdot (\rho \mathbf{U}) = 0 \tag{2}$$

and momentum, neglecting gravitational and body forces,

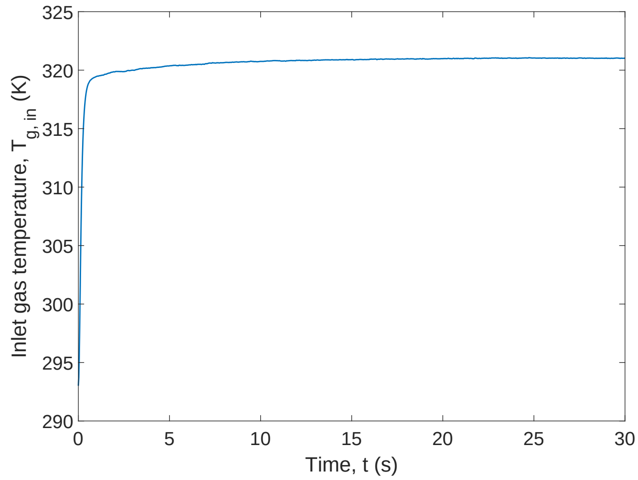

Fig. 3 Inlet gas temperature profile from experiment

$$\frac{\partial \rho \mathbf{U}}{\partial t} + \nabla \cdot (\rho \mathbf{U}\mathbf{U}) = -\nabla p + \nabla \cdot \mu \left[\left(\nabla \mathbf{U} + \nabla \mathbf{U}^T \right) - \frac{2}{3} \nabla \cdot \mathbf{U} I \right] \tag{3}$$

The energy equation, neglecting the effects of viscous heating and internal heat generation,

$$\frac{\partial \rho E}{\partial t} + \nabla \cdot (\rho \mathbf{U} (\rho E + p)) = \nabla \cdot \left(k_{eff} \nabla T \right) \tag{4}$$

where E is the total energy,

$$E = h - \frac{p}{\rho} + \frac{U^2}{2} \tag{5}$$

and k_{eff} $(= k + k_t)$ is the effective thermal conductivity.

The Reynolds averaged forms of these equations were solved, applying the Shear-Stress Transport (SST) turbulence model [20] to model the turbulent kinetic energy k_{tke} and specific dissipation rate ω, from which turbulent viscosity μ_t is computed.

B. Solver set-up and boundary conditions

The rib turbulated passage was simulated using two different methods: quasi-transient modelling the fluid domain in CFD with the solid surface temperature assuming the analytical thermal boundary condition, and steady state CFD with a spatially and temporally constant fixed wall temperature. For both the quasi-transient and steady state methods, the SST turbulence model was chosen, based on extensive comparisons over similar geometries [19]. Pressure and velocity were coupled, and second order upwind spatial discretisation of gradients was used. A constant pressure inlet boundary condition, matched to the specified initial mass flow rate, was implemented. Scaled residuals were monitored as per

Section V.

Inlet turbulence boundary conditions were defined by hydraulic diameter and turbulence intensity. The simulation domain stretched upstream to the location of the experimental heater mesh; this fine mesh removed upstream turbulence, and the 14 hydraulic diameter length between heater mesh and the start of the test section allowed the flow to become naturally fully developed. Inlet turbulence intensity was therefore calculated from the standard correlation for fully developed internal flow,

$$I = 0.16 Re_{D_h}^{-1/8}. \tag{6}$$

The thermal boundary conditions applied by the solver were fixed temperature for both the ATBC and steady state simulations. In the ATBC case, this was a locally resolved (p, z, t) temperature map calculated by external processing assuming semi-infinite 1D heat conduction at each simulation time step (Section IV). For the steady state simulations, a uniform fixed wall temperature for all surfaces was applied (293 K), with an inlet total temperature of 313 K. These temperatures are representative of those used experimentally. Processing was carried out by calculating the heat transfer coefficient with reference to the centreline gas temperature at the same axial location,

$$h(x, y, z) = \frac{\dot{q}(x, y, z)}{T_g(z) - T_w(x, y, z)}. \tag{7}$$

Mean projected rib heat transfer coefficients were calculated by scaling the rib-fluid surface heat transfer coefficient by the ratio of rib wetted surface area (A_s) to rib projected area (A_p),

$$h_p = \frac{\sum h_s A_s}{\sum A_p}, \tag{8}$$

where the summations are carried out over each face cell of a rib. The ratio of rib wetted surface to projected area was 1.49. Gas temperature was calculated from interpolation of the five gas temperature measurement locations as above. Viscosity was calculated using Sutherland's law, using the interpolated gas temperature at each spatial location.

C. Mesh generation and grid independence

Mesh generation was carried out using ANSYS ICEM 15.0. Unstructured meshes were generated from tetrahedral cells, with prism layers grown on the all wall surfaces. Initial prism layer cell heights were: rib = 0.03 mm, pressure/suction surfaces = 0.05 mm, other walls 0.08 mm, which were found to give $y^+ < 1$ across the domain, and were kept constant across all meshes. Four grids, of 3.11-12.9 M cells, were generated. Steady state calculations were run to evaluate the meshes with the following inflow conditions: $T_{g,in}$ = 313 K, $\dot{m}_{g,in}$ = 40 g/s, T_w = 293 K. Total heat transfer rate through the pressure and suction surfaces $\dot{Q}_{PS+SS}$, and mass-averaged static temperature at domain exit $\overline{T_e}$ were assessed (Table 1). It is seen that the convergence for $\overline{T_e}$ is extremely close, with the coarse mesh being < 0.2 %

from the very fine grid. The convergence of $\dot{Q}_{PS+SS}$ was less strong, but the coarse mesh was deemed to be adequate here too (0.8 % absolute difference to the very fine mesh). Based on this assessment, the coarse mesh was used for all simulations reported.

Grid	No. cells M	Prism layer	$\dot{Q}_{PS+SS}$ W	Diff. %	$\overline{T_e}$ K	Diff. %
Coarse	3.11	$N = 8,\ r_e = 1.6$	37.4	0.80	305.4	0.13
Medium	5.38	$N = 15,\ r_e = 1.3$	36.9	2.11	304.7	0.10
Fine	9.52	$N = 15,\ r_e = 1.3$	38.0	0.80	304.91	0.03
V. fine	12.9	$N = 15,\ r_e = 1.3$	37.7	-	305.0	-

Table 1 Mesh independence study reporting percentage difference ('Diff.') to very (v.) fine grid. $\dot{Q}_{PS+SS}$: heat transfer rate through pressure and suction sides (W). $\overline{T_e}$: mass-averaged gas temperature at domain exit (K).N: number of prism layers, r_e: prism layer expansion ratio.

IV. Quasi-Transient Analytic Thermal Boundary Condition

To better approximate the experiment, an analytical boundary condition which simulates the local wall temperature profile temporally was produced. The quasi-transient analytic thermal boundary condition applies the same assumptions made experimentally on the solid wall and the brass ribs: semi-infinite 1D heat conduction, and a lumped thermal mass on top of a semi infinite substrate for the ribs. This method is analogous to that of He and Oldfield [21] for fluctuating flows generated by blade passing events. As the time scales related to the transient fluid flow are extremely small ($t \approx 5 \times 10^{-4}$ s, based on bulk velocity and hydraulic diameter) in comparison to those related to transient heat conduction in the solid (75 s for the thermal pulse to reach the outside boundary of the test section, [1]), there is a large computational cost in accurately simulating the transient nature of the flow with the transient conduction in the solid. Due to this disparity in time scales, the fluid solution is considered steady at each time step.

The calculation of the passage flow solution and the change in surface temperature was done iteratively for a series of equal time steps. Once complete, the heat transfer coefficient distribution was generated. In the following description of the process, index i indicates the time step. Steps 2, 3, 6 were carried out in FLUENT, all others (calculation and post-processing) in MATLAB R2016b.

A. Semi-infinite walls

For all wall surfaces (excluding the rib areas):

1) The heat flux to surface temperature impulse response, H_{q2T_s}, is designed by discrete deconvolution of a $\dot{q}(t) - T_s(t)$ pair [3], from the one-dimensional semi-infinite analytical solution of surface temperature response due to a unit step change in heat flux,

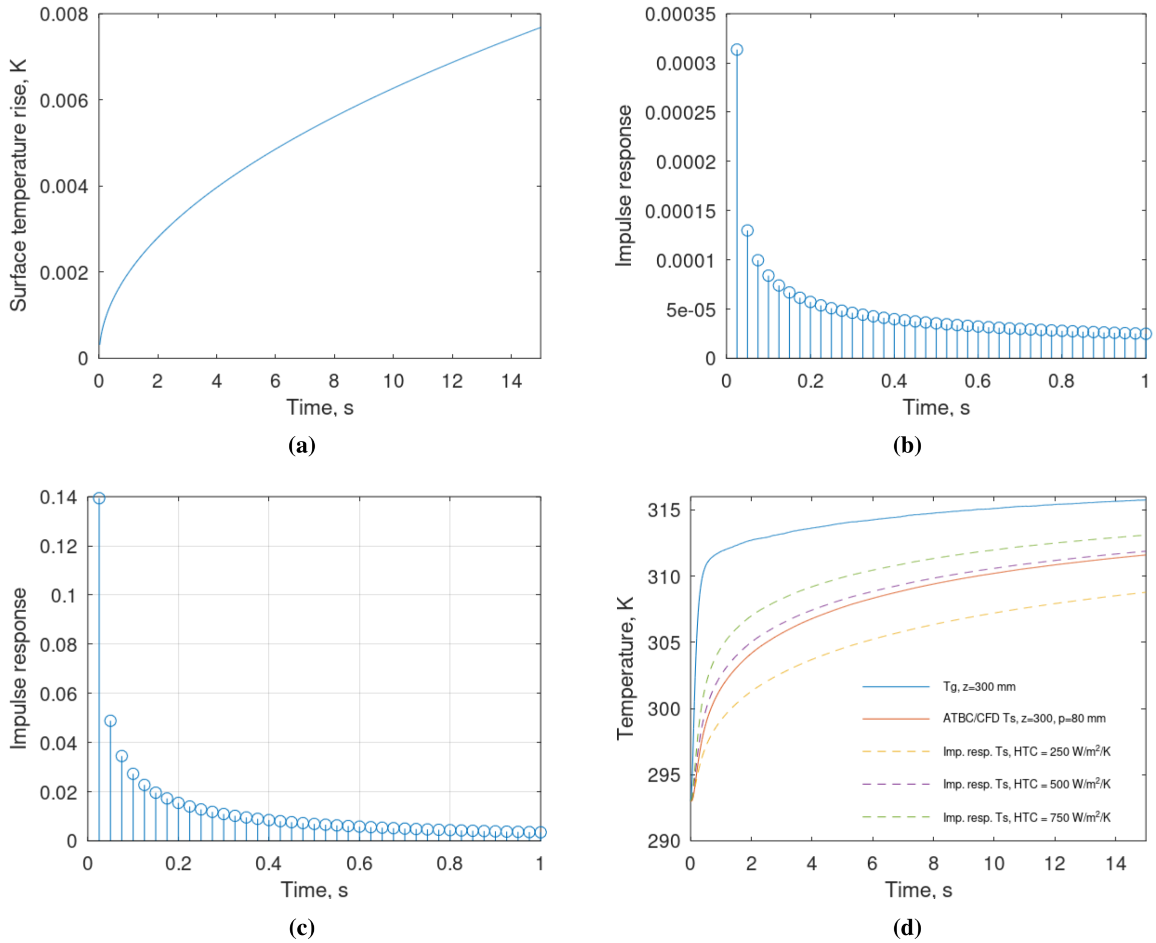

Fig. 4 (a) Perspex surface temperature rise (Eq. 9); (b) Impulse response H_{q2T_s} of perspex; (c) Impulse response $H_{T_g2T_s}$ of perspex to driving gas temperature, (Eq. 12); (d) ATBC/CFD surface temperature history

$$T_s(t) = \frac{2}{\sqrt{\rho_1 c_1 k_1}}\sqrt{\frac{t}{\pi}}, \tag{9}$$

where $\sqrt{\rho_1 c_1 k_1}$ is the thermal product of the solid (Perspex ($\sqrt{\rho_1 c_1 k_1} = 569\frac{W}{m^2 s^{0.5} K}$). This is shown in Fig. 4a for a 1 W/m^2 step in applied uniform heat flux from isothermal conditions. The impulse response, Fig. 4b, shown for one second, is designed by filtering the discrete impulse function, $\delta = 1\,0\,0\,0\ldots$, by the discrete deconvolution of $\dot{q}$ and T_s. Note that the impulse response is calculated for the entire simulated time period.

2) The simulation is initially converged at isothermal conditions, $T_{s,\,i=0} = T_{g,\,i=0} = T_{init}$.
3) The inlet gas temperature is updated to the first step of the experimentally measured temperature profile, $T_{g,\,i=1} > T_{init}$, $T_{s,\,i=1} = T_{init}$, and flow solution reconverged.
4) The surface heat flux at the current time step for the converged solution is read into MATLAB.
5) At each surface location, the surface heat flux time history is then filtered by impulse response H_{q2Ts} (step 1)

using a fast Fourier transform-based filter, which efficiently carries out the discrete convolution process [3]. This gives the surface temperature change due to the change in heat flux at this step. The summation of the impulse responses for the current and all previous steps gives the new surface temperature profile, assuming 1D semi-infinite conduction.

6) The surface temperature profile and next inlet gas temperature are exported to Fluent, and the flow solution is reconverged. Steps 4-6 are iterated until $t = t_{end}$.

For assessment of potential transients, the heat transfer coefficient distribution can be calculated at each spatial location and at each time step based on the heat flux and surface temperatures from the simulation,

$$h\left(t, x, y, z\right) = \frac{\dot{q}\left(t, x, y, z, \right)}{T_g\left(t, z\right) - T_s\left(t, x, y, z\right)}. \tag{10}$$

The centreline gas temperature, $T_g\left(t\right)$, is linearly interpolated between the five axial thermocouple locations as per the experiments. To account for radial conduction in the concave filleted corners of the passage, the general curvature correction method of Buttsworth and Jones [5] was applied,

$$\dot{q} = \dot{q}_{fp} - \frac{\lambda k}{2r}\left(T_s - T_i\right). \tag{11}$$

Here $\dot{q}_{fp}$ is the flat plate heat flux as extracted from the fluid solution, λ is -1 for concave cylindrical surfaces (1 for convex cylindrical surfaces), and k the thermal conductivity of the wall (0.2 W/(m.K) for perspex). This correction is not limited to constant h.

Post-processing of the simulation data is then carried out in an experimental-like manner for direct comparison to the experiments [18]:

7) The surface heat flux and temperature distributions are unwrapped from Cartesian to perimeter-axial ($p - z$) coordinates, giving a 2D surface map as per Figure 2. The maps are regridded to give pixels of uniform size in p, z space.

8) An impulse response from driving gas temperature to surface temperature, $H_{T_g 2 T_s}$, is designed for each axial location in z. Fig. 4c shows this impulse response for a 1 K step in driving gas temperature from isothermal conditions. For an appropriate range of heat transfer coefficient h, for example 0-800 W/m^2/K in 4 W/m^2/K steps, the solution to the 1D Fourier heat equation for the transient surface temperature of a semi-infinite body for a unit step in driving gas temperature is given by

$$T_s\left(t\right) = 1 - \exp\left(\frac{h^2 t}{\rho_1 c_1 k_1}\right)\mathrm{erfc}\left(\frac{h\sqrt{t}}{\sqrt{\rho_1 c_1 k_1}}\right). \tag{12}$$

where erfc is the complex error function. Filtering the impulse function with the deconvolution of the T_g to T_s

pair gives the appropriate impulse response function, similarly to step 1. The temporal centreline gas temperature, T_g varies only in the axial (z) direction.

9) At each axial location the theoretical surface temperature histories is calculated for each value of h defined in step 8 from Equation 12, using the entire centreline gas temperature history at that axial location, convolved with $H_{T_g 2T_s}$, step 8. Three such traces are shown in Fig. 4d, where the actual surface temperature history is compared to the calculated surface temperatures traces for specific values of h (250, 500, and 750 W/m^2/K) at a single location (z=300 mm, p=80 mm). Use of the impulse response method allows an arbitrary gas temperature history to be used, rather than approximating the actual non-ideal step in gas temperature as an ideal step.
10) For each pixel in the p direction at the given z, the sum of squares difference between each theoretical surface temperature history (each h) and the measured temperature history is calculated. This is repeated for each axial position. For Fig. 4d, a final value of HTC = 492 W/m^2/K, Nu = 524, is found.
11) At each pixel, the value of h corresponding to the minimum of the sum of squares differences gives the best fit value of heat transfer coefficient, which is combined into a single, global heat transfer coefficient distribution.

Processing to Nusselt number is done using:

$$Nu(x, y, z) = \frac{h\,(x, y, z)\,D_h}{k} \tag{13}$$

As the experimental post-processing uses the average of TC5 over the test period to calculate the gas thermal conductivity, this is kept consistent in the simulations using:

$$k = 3.0 \times 10^{-14}T^4 - 6.0 \times 10^{-11}T^3 + 8.0 \times 10^{-9}T^2 + 8.7 \times 10^{-5}T + 7.4 \times 10^{-4} \tag{14}$$

where $T = \overline{T_{g,\, z=TC5}}$.

The Nusselt number is normalised by the fully-developed turbulent pipe flow Nusselt number, given by

$$Nu_0 = 0.023 Re_{D_h}^{0.8} Pr^{0.4}, \tag{15}$$

where Re_{D_h} is the bulk Reynolds number based on hydraulic diameter of the passage, and Pr the Prandtl number.

B. Lumped thermal mass on semi-infinite substrate

To account for lateral conduction effects in the ribs, a hybrid rib method, following Wang [4], was implemented. This approach uses a lumped thermal mass for the ribs, implying a uniform material temperature within the rib, from which an equivalent mean heat transfer coefficient can be calculated at the surface of the rib in contact with the passage wall. During the simulation, three processes are considered at each time step: (a) heat convected into the rib, (b) thermal energy rise of the rib, and (c) conduction of heat into the semi-infinite substrate below, equal to the equivalent heat transfer coefficient. Process (c) is calculated using the impulse response from rib temperature to heat flux, the reverse of step 1 (Section IV.A). Taking an energy balance of processes (a-c) allows the rib temperature to be calculated on an iterative basis at each time step. Rib properties were: $\rho_2 = 8490$ kg/m^3, $c_2 = 380$ J/(kg.K), $k_2 = 108$ W/(m.K), $m_2 = 0.63$ g.

A solution to the 1D heat equation is used to produce the impulse response of the hybrid rib-Perspex system, giving the theoretical surface temperature at the rib-Perspex interface (and hence rib-gas interface) for a step change in driving gas temperature, as per Section IV.A. This is based on a two-layer approach following Wang [4]: a high thermal diffusivity layer (rib) on top of the low diffusivity semi-infinite substrate (perspex). For a unit step change in driving gas temperature, the surface temperature response is

$$T_s(t) = 1 - \frac{h}{\beta_2}\frac{1}{b-a}\left[\frac{1}{a}\exp\left(a^2 t\right)\mathrm{erfc}\left(a\sqrt{t}\right) - \frac{1}{b}\exp\left(b^2 t\right)\mathrm{erfc}\left(b\sqrt{t}\right)\right], \tag{16}$$

where

$$a = \frac{\sqrt{\rho_1 c_1 k_1}}{2\beta_2} - \sqrt{\left(\frac{\sqrt{\rho_1 c_1 k_1}}{2\beta_2}\right)^2 - \frac{h}{\beta_2}}, \tag{17}$$

$$b = \frac{\sqrt{\rho_1 c_1 k_1}}{2\beta_2} + \sqrt{\left(\frac{\sqrt{\rho_1 c_1 k_1}}{2\beta_2}\right)^2 - \frac{h}{\beta_2}}, \tag{18}$$

and

$$\beta_2 = \rho_2 c_2 l_2 \left(1 - \frac{h l_2}{2k_2}\right). \tag{19}$$

As the second term on the RHS of Equations 17 and 18 can be complex, a complex error function must be used in Equation 16. The global heat transfer coefficient for each rib is then found by minimising the sum of squares difference between the transient spatial values calculated at each simulation time step and the theoretical solution from Equation 16, as per Section IV.A. Rib HTC values are then inserted into the full HTC distribution (Section IV.A, step 11), replacing the existing rib values, before conversion to Nusselt number.

V. Solution Sensitivities

A. Scaled residuals

The computational cost of the quasi-transient simulations is heavily dependent on the convergence criteria set. The dependence of the solution on the criteria for scaled residual convergence was investigated using a steady state calculation. The total convective heat flux $\dot{q}$ was evaluated at five different convergence limits (Table 2), and compared to the most highly converged solution, case 4. The percentage difference in convective heat flux from the domain, $\dot{q}$, is shown in the final column. Based on this investigation, the case 2 convergence limits were used throughout.

Case	Continuity	$U_{x,\ y,\ z}$	$k,\ \omega$	Energy	Iterations	$\dot{q}$ relative diff.
1	10^{-3}	10^{-3}	10^{-3}	10^{-6}	90	1.4%
2	5×10^{-4}	10^{-6}	5×10^{-5}	10^{-6}	280	0.22%
3	5×10^{-4}	10^{-6}	10^{-5}	10^{-6}	500	0.016%
4	1.1×10^{-4}	10^{-6}	6×10^{-6}	10^{-6}	1000	-

Table 2 Scaled residual criteria with absolute percentage difference in convective heat flux $\dot{q}$ from domain, relative to the most highly converged case (4)

B. Time step

ATBC simulations were carried out using a range of constant time steps: 0.01, 0.025, 0.05, 0.1 s. These simulations were carried out for 1.0 s, which accounts for 94.3% of the inlet gas temperature rise (Figure 3). Simulations were carried out at $Re = 60,000$, using the computational methods described in Section IV.

Area-averaged comparisons of Nusselt number distributions indicated that in relation to the 0.01 s time step, the 0.1, 0.05, 0.025 s simulations had a mean absolute difference of 2.8, 0.9, 0.3% respectively, Figure 5a. Comparisons of the surface temperature rise on the 20$^{\text{th}}$ rib and leading edge are shown in Figure 5b. The displayed values are sampled at the lowest frequency trialled (10 Hz). As the simulation progresses in time, the difference in surface temperature between the varying time steps reduces: a maximum difference of 0.8 K is seen at $t = 0.2$ s, whereas the maximum difference was 0.1 K by $t = 1.0$ s. Relative to the 0.01 s time step, the 0.1, 0.05, 0.025 s simulations were lower by 0.29, 0.11, 0.04%. Based of these assessments, the 0.025 s time step (40 Hz) was therefore chosen, and applied to the ATBC simulations.

VI. Results

A. Mass flow rate and Reynolds number

The variation of mass flow rate and Reynolds number with time is shown in Figure 6. The simulation exhibits a similar temporal drop in mass flow rate profile as the experiment, however the decrease in mass flow rate is 3.9 % in comparison to 1.1 % seen in the simulation. Similarly, the Reynolds number shows a similar trend, with the simulation decreasing by 4.0 % in comparison to experimental 7.1 %. This switch is due to differing values of μ_g due to different gas temperatures simulated relative to the experimental work, and the inlet/outlet boundary conditions implemented. These were deemed acceptable as they fall within the experimental uncertainties.

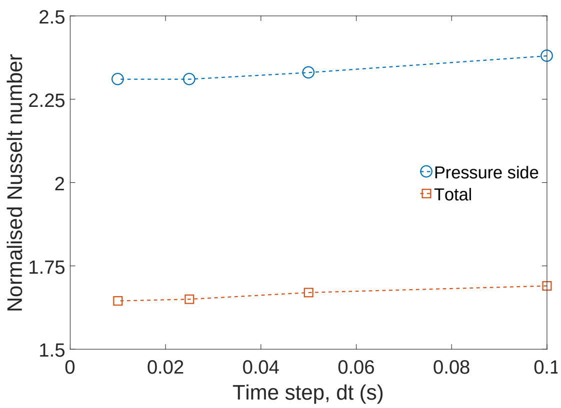

(a)

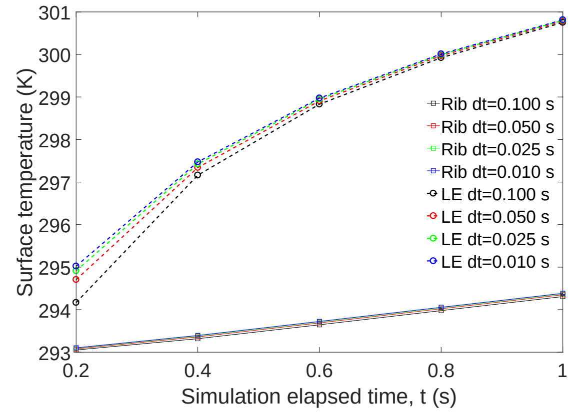

(b)

Fig. 5 Summary of investigation into effect of time step on ATBC simulations. (a) Area-averaged normalised Nusselt number on pressure side and total area. (b) Surface temperature rise on 20th rib and leading edge (LE).

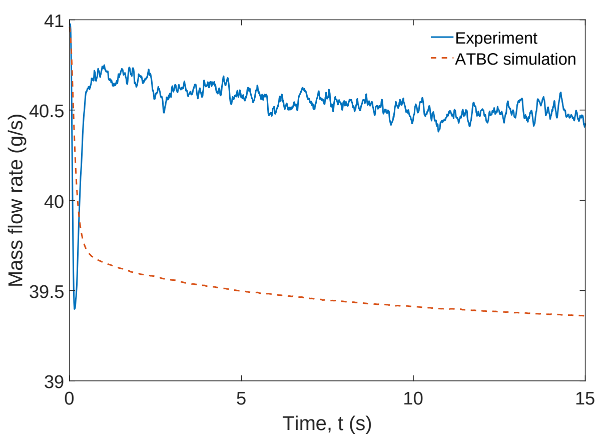

(a) Mass flow rate with time

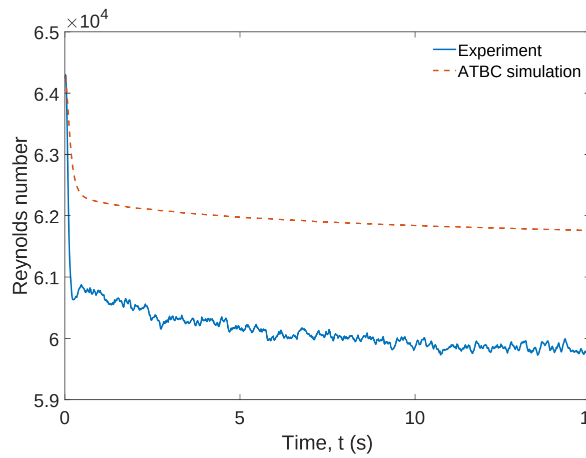

(b) Bulk Reynolds number with time

Fig. 6 Variation of mass flow rate and Reynolds with time for experiments and ATBC simulation.

B. Gas temperature profiles

Figure 7 shows comparisons between experimental and simulated gas temperature profiles. Figure 7a shows pointwise gas temperature profiles with time, for thermocouples different axial locations: start (TC1), z = 12.5 mm; middle (TC3), z = 226 mm; end (TC5), z = 422 mm. Axial position z = 0 mm corresponds to first rib location. For the TC1 and TC5 locations, the simulation is able to well-predict the experimental temperature. A small disparity (8.4 % of temperature difference $T_{g5} - T_i$) is seen in the TC5 trace in the first second, indicating the transient behaviour is not fully captured. The middle thermocouple, TC3, is not well simulated. The reason for the discrepency at TC3 can be seen in the streamwise gas temperature comparisons, Figure 7b. Here it is observed that the simulations predict a 'trough' in gas temperature in the middle region axially of the passage (z = 150 – 220 mm), followed by a recovery (z = 220 – 400) mm. This has been previously described as the initial roll up of the secondary flows before sweeping across the passage [19]. The presence of this trough and recovery is a phenomenon seen experimentally, with its exact streamwise location being highly influential on the interpolated gas temperature profile.

Linearly interpolated gas temperature profiles, taken at the experimental thermocouple locations, are seen in Figure 7c. Whilst the streamwise profiles show that the temperature recovery location is highly influential, the profiles indicate that the quasi-transient ATBC simulations are able to capture changing centreline gas temperature with time. As the simulation progresses, it is observed that the profiles become more uniform: the ATBC simulation captures the transient heating of the passage walls, leading to a smaller fall in centreline gas temperature down the passage in the later stages of the simulation. The centreline gas temperature as used in the steady-state simulations is also shown. It is observed that this is less representative of the gas temperature profile at the end of the experiments in comparison to the ATBC simulations, as this transfer of heat from gas to wall has not been accounted for.

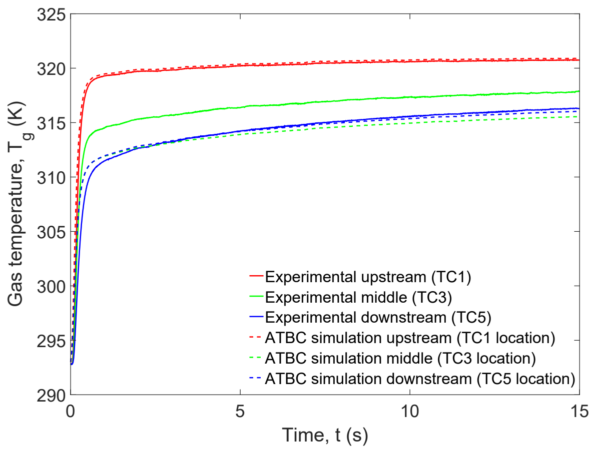

(a) Thermocouple location histories

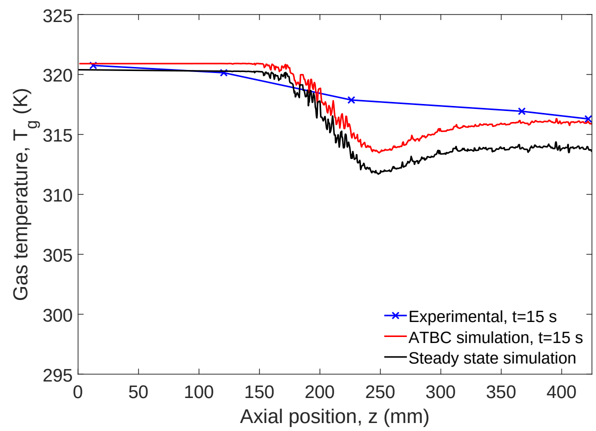

(b) Linearly extrapolated streamwise distribution

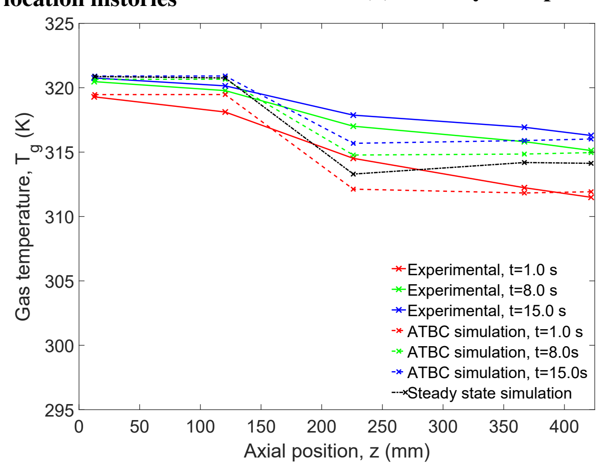

(c) Linearly extrapolated streamwise distribution

Fig. 7 Comparison of centreline gas temperature between the experiment and both quasi-transient ATBC and steady-state simulations.

C. Nusselt number distributions

Nusselt number distributions for the analytic boundary condition and steady state simulations are shown against the experimental data in Figure 8. Surface names (suction side, trailing edge, pressure side, leading edge) are as Figure 2. As no experimental rib values are available for the suction side, this surface is excluded from the following discussion.

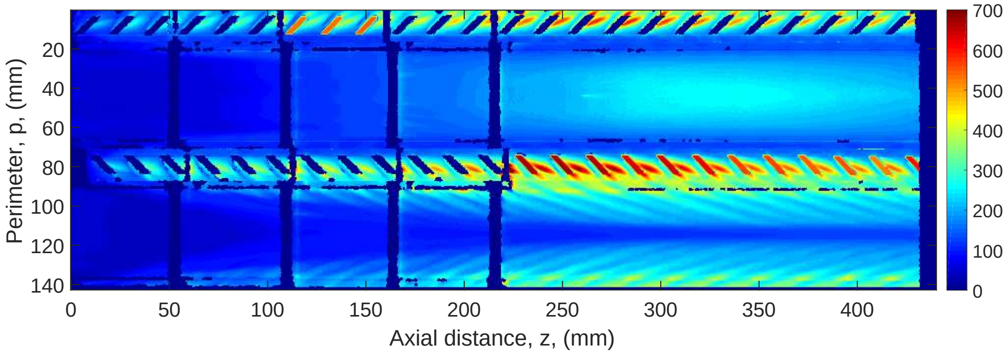

(a) Experimental

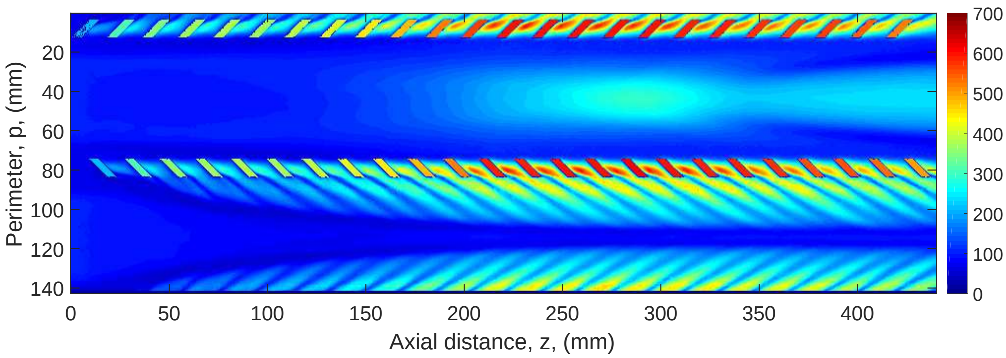

(b) CFD: Analytical thermal boundary condition, ATBC

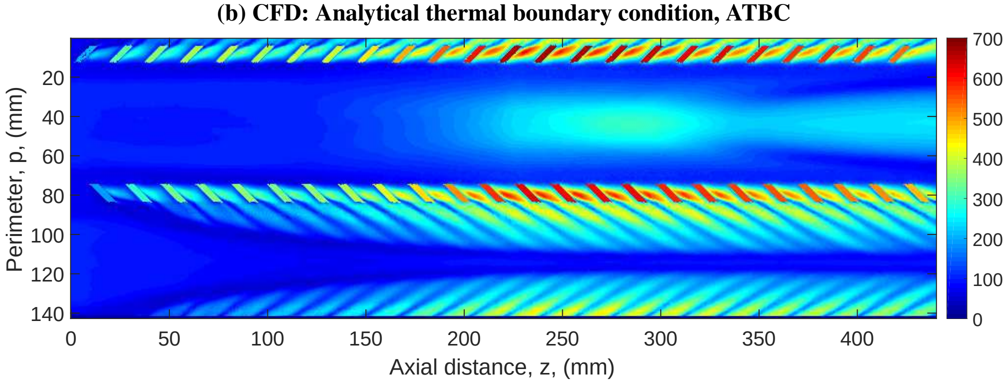

(c) CFD: Steady state

Fig. 8 Nusselt number distributions for experiment, analytic boundary condition, and steady state simulations.

The ATBC simulation (Figure 8b) is observed to be a reasonable match to the experimental data. The spatial mean absolute difference was found to be 21.6% across the downstream half of the map (z > 220 mm). The mean difference in area-averaged Nusselt number was 8.6% below experimental. On the pressure surface, the mean absolute difference to experimental rib Nusselt number values was 6.4%, with the trend, peaking ribs 12-17, then falling, well captured.

The steady state simulation results, Figure 8c, is observed to be extremely similar to the ATBC distribution. The spatial mean absolute difference was 20.5%, with an area-averaged difference of 7.1% below experimental levels, both closer to the experimental data than the ATBC simulations. The rib levels were less well predicted than the ATBC method, 6.6% difference.

These results show that the steady state and quasi transient method give very similar Nusselt number distributions. From this we see that any variation in HTC or Nusselt number with time using the transient methods is negligible when the final distributions are calculated.

Following the discussion in [17] regarding the variation of heat transfer coefficient with time during a transient test, Figure 9 plots axial profiles of Nusselt number with time. The underlying HTC maps are constructed using Equation 10. Two locations are used: in the middle of the pressure surface ($p = 80$ mm) and the middle of the trailing edge ($p = 45$ mm). Both locations are shown as absolute Nusselt number (plots (a) and (c)), and as percentage difference to final value Nusselt number at $t = 15.0$ s, given as a percentage (plots (b) and (d)), $\left(Nu\left(t\right) - Nu_{t=15.0\,\mathrm{s}}\right)/Nu_{t=15.0\,\mathrm{s}}$. The rib values, flat regions in (a) and (b), should be disregarded as the hybrid rib processing is carried out after this point in the method.

A number of interesting features are seen. The Nusselt number distribution is seen to vary somewhat with time on both the pressure side and trailing edge. On the pressure surface, Figures 9a and 9b, the variation is largest in the developing region of the passage, $z < 220$ mm. This is seen to be up to 43% at $t = 1.0$ s relative to $t = 15.0$ s. By $t = 5.0$ s the maximum difference is seen to fall to 18%. In the region of the passage where the secondary flow vortices are seen to coalesce and impinge the trailing edge ($250 < z < 310$ mm, see Figure 8b and discussion in [9, 22]), the variation of Nu with time is significantly lower, peaking at 12% difference, and quickly converging to < 5% difference. This is potentially due to the better mixing of the flow in this region. Moving downstream, $z > 310$ mm, the variation with time increases to a maximum of 21% at $t = 1.0$ s, and 8% by $t = 5.0$ s.

On the trailing edge, the variation of Nusselt number with time is significantly lower. This is clearly seen from Figure 9c. Peak values of 12% are seen in the early developing flow region ($z < 10$mm), however convergence towards a steady value is rapid for most of the passage: for $z > 25$ mm, by $t = 5.0$ s all of the passage is below 2.5% difference to the $t = 15.0$ s solution.

Area-averaging the Nusselt number at every time step was carried out. It was observed that the transients have a small effect on the mean value; the area-averaged value converged to within 0.5% of its steady final value within 0.2 s. It was also observed that the global minimisation process applied to match simulated surface temperatures against theoretical surface temperatures, generated from a range of h (Eq. 12), is not significantly affected by the transient variation of spatial HTC or Nu. Whilst this transient behaviour is noted, it is not significantly affecting the global results.

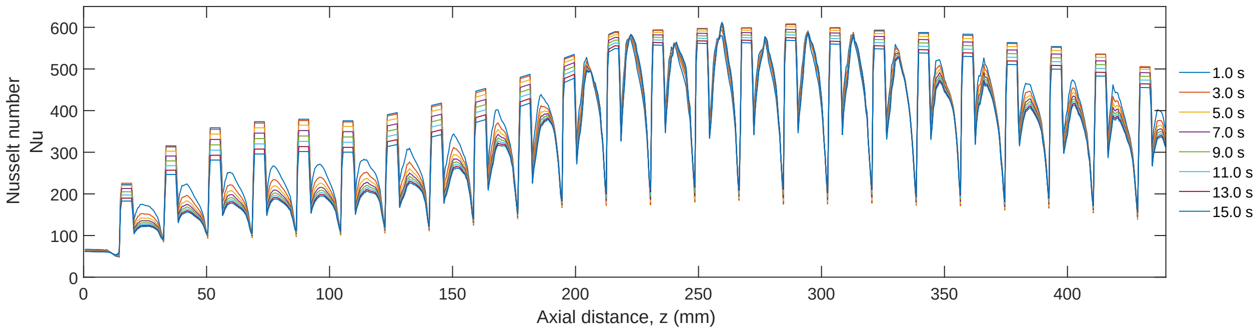

(a) Mid-pressure side

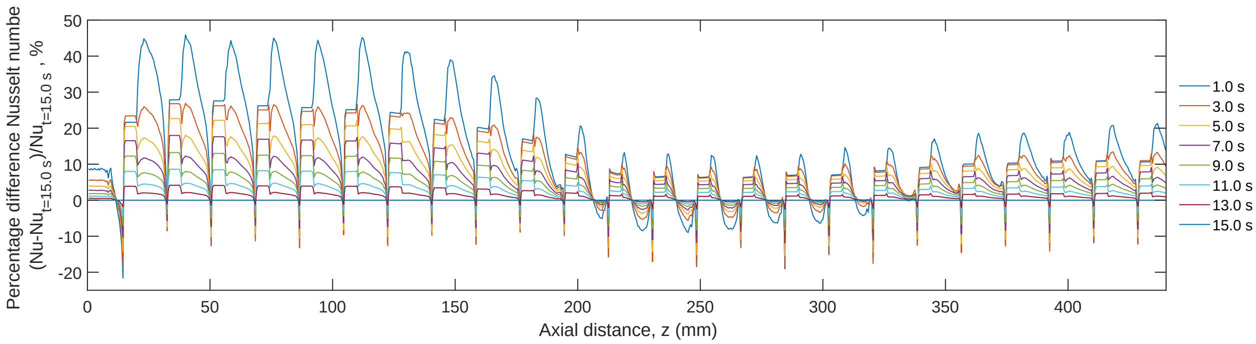

(b) Mid-pressure side, normalised against $Nu_{t=15.0\ \mathrm{s}}$

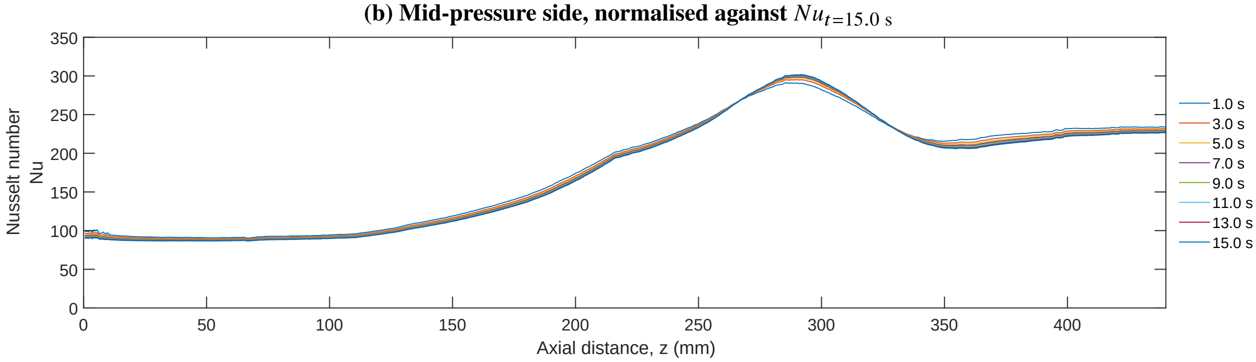

(c) Mid-trailing edge

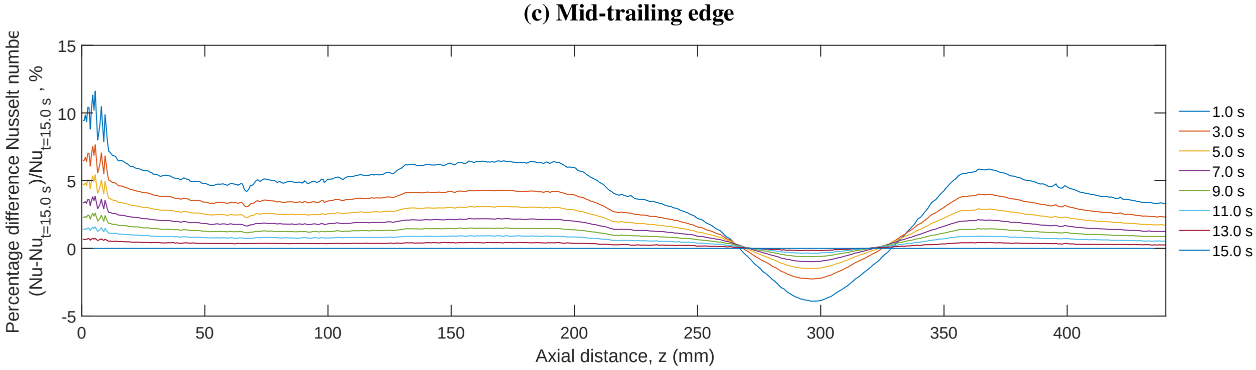

(d) Mid-trailing edge, normalised against $Nu_{t=15.0\ \mathrm{s}}$

Fig. 9 Variation and percentage difference of Nusselt number with time for (a,b) mid-pressure side (p = 80 mm,), and (c,d) mid-trailing edge (p = 45 mm) from ATBC simulations.

D. Influence of Reynolds number

Further simulations were carried out at $Re = 19,000, \; 107,000$ for the same aspect ratio passage using the quasi-transient ATBC and steady state methods. The same inlet temperature profile was used. The area-averaged normalised Nusselt numbers are shown in Figure 10 for the trailing and leading edges, and pressure surface. Averaging is carried out over the downstream half of the passage.

On the trailing edge the steady state simulations are seen to reproduce the experimental results more closely at all three Reynolds number cases. A maximum disparity of 27.4% is seen for quasi-transient ATBC method, and 21.2% for the steady state, both at $Re = 19,000$. The two methods are seen to converge with increasing Reynolds number.

On the leading edge the performance of the two calculation methods is more similar than on the trailing edge. Maximum differences of 10.8% and 15.1% are seen for the ATBC and steady state methods respectively. Qualitatively the ATBC simulations reproduce the trend seen experimentally with greater fidelity.

On the pressure side the ATBC method reproduced the experimental values more closely, though the performance of the methods is quantitatively similar: absolute differences for the ATBC method range 10.6-13.3%, and 10.6-17.3% for the steady state simulations. Neither method well-captures the qualitative trend of decreasing normalised Nusselt number with increasing Reynolds number.

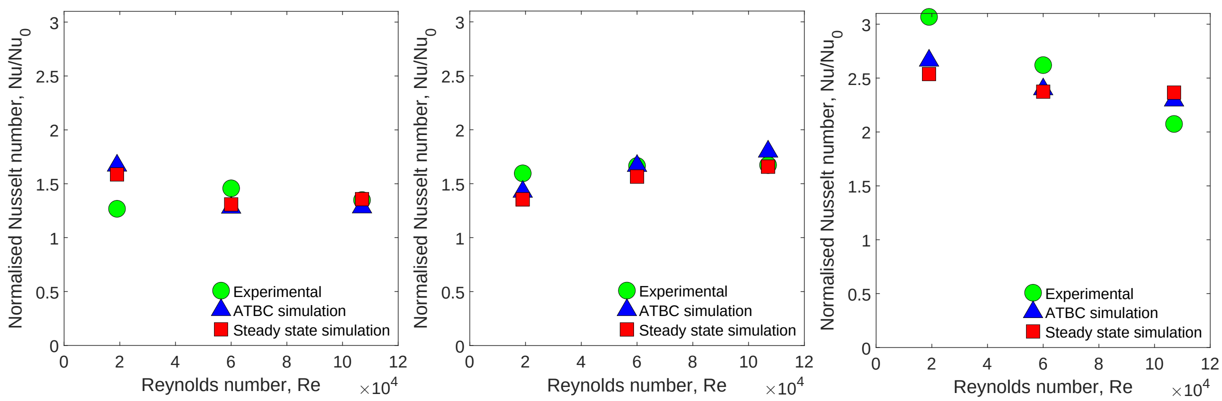

(a) Trailing edge **(b) Leading edge** **(c) Pressure side**

Fig. 10 Area-averaged normalised Nusselt number. Normalisation done by smooth pipe Nusselt number correlation (Equation 15).

VII. Conclusion

A new method for the direct simulation of transient thermochromic liquid crystal experiments has been implemented. On an iterative basis the surface heat flux from steady state simulations is used to calculate the surface temperature as a series of impulse responses. The new surface temperature is then applied as a boundary condition to the simulation and the fluid re-solved. A transient inlet gas temperature profile was applied. This quasi-transient analytical temperature boundary condition method is able to capture the changing streamwise gas temperature profile with time, as seen experimentally, which was thought to be a key driver for the disparity between previous steady state simulations and experiments, demonstrating that this not infact the case.

Simulations carried out using the ATBC and steady state methods indicated that the two methods performed very similarly across the range of conditions undertaken. Transient variation of the Nusselt number distributions were noted at some locations. In the early stages of the simulations, $t \leq 1.0$ s, these variations were up to 40% relative to the end value ($t = 15.0$ s) in the developing flow region. The variation was seen to quickly reduce with increasing simulation time. Away from the ribbed walls the transient differences in Nusselt number were seen to be small (< 5%), and passage-averaged values of Nusselt number converged within 0.5% of their final value after 0.2 s. It can therefore be inferred that the use of appropriate processing techniques can significantly reduced the effect of initial transient HTC values.

Further development of the method will include expanding the range of turbulence modelling applied, and investigations into the root causes of the transient behaviour noted of heat transfer coefficient/Nusselt number distributions.

Acknowledgments

This research could not have been undertaken without the support of Christian Orozco-Pineiro and his insightful discussions throughout the EU-funded ERICKA programme.

References

[1] Shultz, D. L., and Jones, T. V., “Heat transfer measurements in short-duration hypersonic test facilities,” AGARDograph 165, 1973.

[2] Ireland, P. T., and Jones, T. V., “Liquid crystal measurements of heat transfer and surface shear stress,” *Measurement Science Technology*, 2000, pp. 969–986. https://doi.org/https://doi.org/10.1088/0957-0233/11/7/313.

[3] Oldfield, M. L. G., “Impulse Response Processing of Transient Heat Transfer Signals,” *Journal of Turbomachinery*, Vol. 130, 2008, pp. 021023–1/9. https://doi.org/https://doi.org/10.1115/1.2752188.

[4] Wang, Z., “The Application of Thermochromic Liquid Crystals to Detailed Turbine Blade Cooling Measurements,” D. Phil. Thesis, University of Oxford, 1991.

[5] Buttsworth, D. R., and Jones, T. V., “Technical note: Radial conduction effects in transient heat transfer experiments,” *Aeronautical Journal*, Vol. 101, No. 1005, 1997, pp. 209–212. https://doi.org/https://doi.org/10.1017/S0001924000066380.

[6] Ling, J. P., Ireland, P. T., and Turner, L., “A Technique for processing transient heat transfer, liquid crystal experiment in the presence of lateral conduction,” , 2004. https://doi.org/https://doi.org/10.1115/1.1740777.

[7] Coletti, F., Scialanga, M., and Arts, T., “Experimental investigation of conjugate heat transfer in a rib-roughened trailing edge channel with crossing jets,” , April 2011. https://doi.org/https://doi.org/10.1115/1.4003727.

[8] Ryley, J. R. and McGilvray, M. and Gillespie, D. R. H., “Heat Transfer Coefficient Determination on 3D Geometries from Transient Thermochromic Liquid Crystal Experiments,” *Journal of Thermophysics and Heat Transfer (Published Online)*, 2019. https://doi.org/https://doi.org/10.2514/1.T5701.

[9] Forsyth, P., McGilvray, M., and Gillespie, D. R. H., “Secondary flow and heat transfer coefficient distributions in the developing flow region of ribbed turbine blade cooling passage,” *Experiments in Fluids*, Vol. 58, No. 5, 2017, pp. 1–15. https://doi.org/https://doi.org/10.1007/s00348-016-2286-6.

[10] Gillespie, D. R. H., Byerley, A. R., Ireland, P. T., Wang, Z., Jones, T. V., and Kohler, S. T., “Detailed Measurements of Local Heat Transfer Coefficient in the Entrance to Normal and Inclined Film Cooling Holes,” *Journal of Turbomachinery*, Vol. 118, No. 2, 1996, pp. 285–290. https://doi.org/10.1115/1.2836638, URL https://doi.org/10.1115/1.2836638.

[11] O’Dowd, D., Znag, Q., He, L., Ligrani, P., and Friedrichs, S., “Comparison of Heat Transfer Measurement Techniques on a Transonic Turbine Blade Tip,” *Journal of Turbomachinery*, Vol. 133, No. 2, 2011, pp. 021028–1/10. https://doi.org/https://doi.org/10.1115/1.4001236.

[12] Gillespie, D., “Intricate Internal Cooling Systems for Gas Turbine Blading,” DPhil thesis, University of Oxford, 1996.

[13] Camci, C., Kim, K., and Hippensteele, S., “A new hue capturing technique for quantitative interpretation of liquid crystal images used in convective heat transfer studies,” *Journal of Turbomachinery*, Vol. 114, 1992, pp. 765–775. https://doi.org/https://doi.org/10.1115/1.2928030.

[14] Ireland, P., Neely, A., Gillespie, D., and Robertson, A., “Turbulent heat transfer measurements using liquid crystals,” *International Journal of Heat and Fluid Flow*, Vol. 20, No. 4, 1999, pp. 355–367. https://doi.org/https://doi.org/10.1016/S0142-727X(99)00030-2.

[15] Cukurel, B., and Arts, T., “Local Heat Transfer Dependency on Thermal Boundary Condition in Ribbed Cooling Channel Geometries,” *Journal of Heat Transfer*, Vol. 135, No. 10, 2013, pp. 101001–1/11. https://doi.org/https://doi.org/10.1115/1.4024494.

[16] Maffulli, R., and He, L., “Impact of Wall Temperature on Heat Transfer Coefficient and Aerodynamics for Three-Dimensional Turbine Blade Passage,” *Journal of Thermal Science Engineering and Applications*, Vol. 9, No. 4, 2017, pp. 041002–1/12. https://doi.org/https://doi.org/10.1115/1.4036012.

[17] Sathyanarayanan, S., and Shih, T.-P., “Time-Accurate Conjugate Analysis of Transient Measurements of Heat Transfer Coefficients,” *Journal of Thermophysics and Heat Transfer*, Vol. 31, No. 3, 2017, pp. 527–537. https://doi.org/https://doi.org/10.1016/j.jppr.2013.01.003.

[18] Ryley, J. R. and McGilvray, M. and Gillespie, D. R. H., “Local Heat Transfer Coefficient Measurements on an Engine-Representative Internal Cooling Passage,” *Journal of Thermophysics and Heat Transfer*, Vol. 33, No. 1, 2019, pp. 189–198. https://doi.org/https://doi.org/10.2514/1.T5206.

[19] McGilvray, M., Orozco Pieiro, C., Axe, T., Ryley, J., and Gillespie, D. R. H., “Comparison of Stationary Internal Cooling Passage Experimental Data to Numerical Simulations,” 10th European Conference on Turbomachinery, Fluid Dynamics and Thermodynamics, 2013.

[20] Mentor, F., “Two-Equation Eddy-Viscosity Turbulence Models for Engineering Applications,” *AIAA Journal*, Vol. 32, No. 8, 1994, pp. 1598–1605. https://doi.org/https://doi.org/10.2514/3.12149.

[21] He, L., and Oldfield, M. L. G., “Unsteady Conjugate Heat Transfer Modelling,” *Journal of Turbomachinery*, Vol. 133, 2011, pp. 031022–1/12. https://doi.org/https://doi.org/10.1115/1.4001245.

[22] McGilvray, M., Ryley, J., and Gillespie, D. R. H., “Investigation of wrapping ribs onto smooth walls for mid-chord internal cooling passages,” ASME Turbo Expo, Paper GT2014-26800, 2014. https://doi.org/https://doi.org/10.1115/GT2014-26800.